Optics Letters

Ultrafine intravascular photoacoustic endoscope with a 0.7 mm diameter probe

PENG LEI,[1,2,3] XUE WEN,[1,2] LEI WANG,[2] PENGFEI ZHANG,[4,5,6] AND SIHUA YANG[1,2,3,7]

[1]MOE Key Laboratory of Laser Life Science & Institute of Laser Life Science, South China Normal University, Guangzhou 510631, China
[2]College of Biophotonics, South China Normal University, Guangzhou 510631, China
[3]Guangdong Provincial Key Laboratory of Laser Life Science, South China Normal University, Guangzhou 510631, China
[4]Department of Cardiology, Qilu Hospital of Shandong University, Jinan 250012, China
[5]Key Laboratory of Cardiovascular Remodeling and Function Research, Chinese Ministry of Education and Chinese National Health Commission Shandong University, Jinan 250100, China
[6]e-mail: pengf-zhang@163.com
[7]e-mail: yangsh@scnu.edu.cn

Received 13 September 2019; revised 29 September 2019; accepted 5 October 2019; posted 11 October 2019 (Doc. ID 377640); published 6 November 2019

Intravascular photoacoustic (IVPA) imaging, benefiting from high optical contrast, large imaging depth and absorption specificity, is of great potential for lipid-rich plaque detection. However, the diameters of reported IVPA endoscopes are too big to intervene into the coronary artery branches. Here, by designing an ultracompact house embedded with a side-fire fiber and a miniature single-element ultrasound transducer, we developed an ultrafine IVPA endoscope with a diameter of 0.7 mm aiming at coronary artery branches atherosclerotic plaque detection. The reliability and feasibility of the ultrafine IVPA endoscope was demonstrated by imaging a stent with a 1.6 mm inner diameter. Furthermore, the photoacoustic imaging and ultrasound imaging of a mouse thoracic aorta with an inner diameter of 1.15 mm was conducted to verify the clinical potentiality of the endoscope, and the PA images have good consistency with histological staining results. To the best of our knowledge, this is the first time we have achieved the IVPA imaging in fine vessel by the 0.7 mm diameter ultrafine photoacoustic endoscope, which paved a way for the translation of the IVPA endoscope to clinical application.

https://doi.org/10.1364/OL.44.005406

Coronary artery diseases, caused by atherosclerotic plaque rupture and subsequent thrombosis, remain the leading factors of morbidity and mortality throughout the world [1]. Photoacoustic imaging (PAI) is a rapidly developing technique capable of providing anatomic, functional, and molecular information about biological tissue, which can provide volumetric images with high optical contrast and high ultrasonic spatial resolution at sufficient imaging depths [2–11]. Intravascular photoacoustic (IVPA) imaging has been one of effective methods for quantitative assessment of plaque lesions and mapping the lipid distribution over the entire artery wall [12–16]. The ongoing development of IVPA endoscopes has focused on improving the imaging speed, achieving high spatial resolving ability, and combining them with other intravascular imaging methods. Various fast optical parametric oscillator (OPO) lasers, new beam focusing methods and other mixed technologies related to the IVPA system have emerged within the past few years [17–24]. However, the diameter of an IVPA probe is still one of the factors that limit the IVPA endoscope for coronary artery branches detection. Coronary artery branches, such as the anterior descending branch from the main coronary artery to the circumflex branch, are usually characterized by exceedingly small diameters. When stenosis takes place in those branches, the acute coronary syndromes would occur with high probability. Therefore, the miniaturization of the IVPA endoscope is of great significance for the detection of coronary artery branches atherosclerotic lipid-rich plaque. In this circumstance, the ultrafine IVPA endoscope has the advantage of lipid detection.

In this Letter, we present the design of an ultrafine IVPA endoscope with an ultracompact house, a side-fire fiber (SFF) and a miniature single-element transducer. The SFF with an angle of 35° and coated with gold film at the polished end was used for the delivery of light to the probe. The core diameter of the SFF was 50 μm, and the total diameter of the fiber was 144 μm. The miniature single-element ultrasound transducer with the dimension of 0.5 mm × 0.6 mm × 0.3 mm (customized, Doppler, Guangzhou, China) was used for PA signals reception. The design of the ultrafine endoscope with a diameter of 0.7 mm is shown in Fig. 1(a). The SFF and the transducer cable were installed through the two channels of the 0.7 mm diameter house, and the transducer was fixed on the platform of the house. The transducer was fixed forward the SFF, with its sensing area facing the laser emit direction. Then, the 0.7 mm ultracompact house embedded with the SFF and the miniature ultrasound transducer was connected to a 0.7 mm diameter torque coil (customized, Asahi Intecc, Aichi, Japan). The assembled 0.7 mm probe is shown in

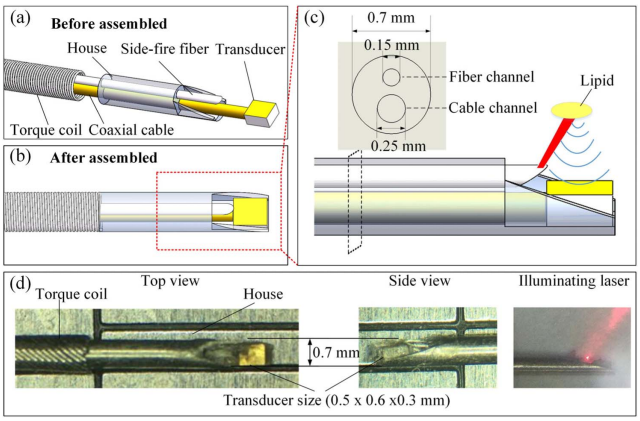

Fig. 1. Design and photograph of the 0.7 mm ultrafine IVPA endoscope. (a) Main components of the probe before being assembled. (b) Assembled 0.7 mm probe. (c) Zoom-in view of the probe tip with emit laser and excited ultrasonic waves. The upper left corner was the cross-section structure of the house. (d) Photograph of the fabricated 0.7 mm probe and the illuminating laser (at 680 nm) from the probe.

Fig. 1(b). The zoom-in view of the 0.7 mm probe and the detailed design of the ultracompact house were shown in Fig. 1(c), and the upper left showed the detailed cross section structure of the ultracompact house. Figure 1(d) shows the photographs of the probe from the top view and the side view, along with the illuminating laser from the probe, since the laser at 1720 nm is invisible; 680 nm was chosen to show the laser emission path of the probe.

The intensity distribution of the emitted laser beam, measured by the beam analyzer at 1 mm distance from the SFF polished end, is shown in Fig. 2(a). The intensity curve [inset of Fig. 2(a)] exhibited the diameter of the spot, which was about 200 μm. The miniature transducer has a central frequency of 50 MHz, and the spectrum curve of the transducer is shown in Fig. 2(f). The ultrafine probe was connected to the

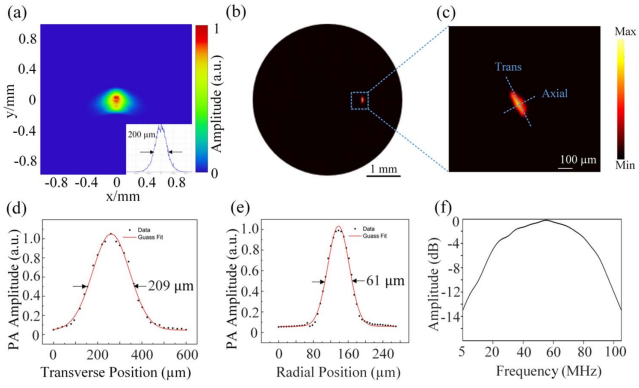

Fig. 2. Lateral and axial resolution of the ultrafine IVPA endoscope. (a) The emitted laser beam intensity distribution of the SFF measured by the beam analyzer, and the bottom right corner is the measured laser spot curve. (b) The B-scan IVPA image of a carbon fiber (7 μm in diameter). (c) Enlarged view of the dashed box in (b). (d) The lateral resolution of the ultrafine endoscope. (e) The axial resolution of the ultrafine IVPA endoscope. (f) The bandwidth of the miniature single-element ultrasound transducer.

IVPA/US imaging system to rotate and acquire the PA/US signals. An OPO laser source (NT200 Series Laser, Ekspla, Vilnius, Lithuania) was used to deliver a high repetition pulsed laser at a rate of 2.5 kHz, and the duration of the laser was approximately 8 ns. The laser at 1720 nm, which was highly absorbed by lipid, was used to conduct the experiments. The laser beam was first collimated, then focused by a convex lens and passed through a 50 μm pinhole for spatial filtering. Subsequently, the reshaped laser was focused into the fiber by an objective lens (RMS4X, Thorlabs, USA), which was fixed in a Travel Flexure Microblock MBT Series Stage (MBT613D, Thorlabs, USA). The fiber was connected to the stator end of an optical-electric slip ring (customized, JINPAT, China). Finally, the laser was delivered to the probe by the SFF. The output energy from the fiber tip was about 32 μJ, and the energy density was calculated to be $0.1 J/cm^2$, which was below the 1 J/cm^2 ANSI safety standard at this wavelength. The PA signals excited by the pulse laser were transmitted by the optical-electric slip ring mentioned above. The three-dimensional (3D) images of the samples were obtained by the rotation motor and the retraction motor [25].

The induced IVPA/US data detected by the ultrasound transducer were first pre-amplified by the pulse generator/receiver (5073PR, Olympus, USA) with a 10 dB gain, and then the raw data was amplified by the main amplifier (LNA-650, RFBAY, Gaithersburg, MD, USA) with a 53 dB gain and digitized by a high-speed data acquisition card (M-3i.4120, Spectrum, German) at a sampling rate of 250 MHz/s. All the procedures were controlled by the Labview software (National Instrument, USA), and the data reconstruction was processed by MATLAB (MathWorks, USA).

To evaluate the spatial resolution of the ultrafine endoscope, imaging of a carbon fiber with strong optical absorption and a well-defined thin diameter was conducted. The carbon fiber, with a diameter of 7 μm, was positioned parallel to the probe within an agar phantom. And the distance between the probe and the carbon fiber was about 1.0 mm. Figure 2(b) showed the reconstructed cross-sectional PA image of the carbon fiber with a rotational scanning, as the bright spot observed in the view. The enlarged PA image of the carbon fiber is shown in Fig. 2(c). The experimental data of the imaged carbon fiber was plotted along the radial direction and the transverse direction, respectively. The dotted lines were then fitted with Gaussian functions to estimate the lateral resolution and the axial resolution. Based on the full width at half-maximum (FWHM) of the fitted functions, the lateral resolution was estimated to be 209 μm, while the axial resolution was 61 μm, as shown in Fig. 2(d) and Fig. 2(e), respectively.

In the proof-of-concept experiment, the feasibility of the ultrafine probe was first verified by imaging a fine stainless-steel cardiovascular stent with an inner diameter of 1.6 mm. The stents were widely used when the vascular was stenotic. The endoscope with the finer diameter was easier to intervene into the stent, facilitating the observation of stent expansion and apposition. In our experiments, the stent was fixed in agar phantom, and the probe was put in the center of the stent. Five hundred A-lines were acquired to reconstruct a cross-sectional PA image. The imaging planes were moved axially from proximal to distal of the stent with the spatial distance of 200 μm using the retraction motor. Two hundred and fifty cross-sectional PA images were acquired to reconstruct the 3D

image of the stent. The photograph of the stent is shown in Fig. 3(a). Since the stent was not completely same from the proximal to the distal, three representative cross sections (the white dash lines labeled as I, II, III) were chosen to test the ability of the endoscope. Figure 3(b) exhibited the corresponding PA images of the three chosen cross sections. The cross-section I PA image showed the even spacing wire of stent. The cross-section II PA image displayed the stent junction of two wires and that was why the least bright spot in the PA image, and the cross-section III PA image depicted the largest spacing wire of stent. The 3D PA image of the stent reconstructed by Volview (Kitware, USA) was also displayed in Fig. 3(c). The cross-sectional images and the 3D PA images showed good morphology of stent, which indicated that the endoscope can be performed post-intervention to guide the situation of the stent.

To verify the performance of the ultrafine probe in fine vessel-mimicking sample with lipid core, PA imaging of the porcine adipose tissue in fine tubular was conducted. The porcine adipose tissue was put into a tube with an inner diameter of 1.6 mm [Fig. 3(d)], and the endoscope was employed to detect lipid-rich plaque spatial structure in a fine vessel. The experiment was conducted as described above. Figure 3(d) exhibited the photograph of the fine tubular sample with a lipid core. Three different cross sections [marked as i, ii, iii by green dash line in Fig. 3(d)] of the sample were chosen to display the PA images. Figure 3(e) showed the corresponding cross-sectional PA images of the sample marked in Fig. 3(d); the PA images of the three sections were diverse from each, just as the photograph showed. The 3D PA image of the fine vessel-mimicking sample with a lipid core is also reconstructed and shown in Fig. 3(f). The spatial structure of the fine vessel-mimicking sample with a lipid core was clearly observed. The good contrast 3D images of stent and the fine vessel-mimicking sample with a lipid core demonstrated the reliability and feasibility of the ultrafine IVPA endoscope.

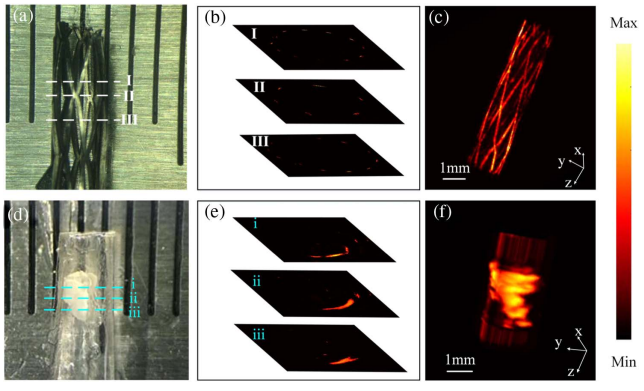

Fig. 3. IVPA endoscope imaging of the stent and the fine vessel-mimicking sample with lipid core. (a) Photograph of the stent with an inner diameter of 1.6 mm; the scale of the ruler is 1.0 mm. (b) Corresponding cross-sectional PA images of the stent marked in (a). (c) 3D PA image of the stent in (a); the scale bar is 1.0 mm. (d) Photograph of the fine vessel-mimicking sample with lipid core. (e) Corresponding cross section PA images of the sample marked in (d). (f) 3D PA image of the fine vessel-mimicking sample with lipid core.

To further verify the advantage of the ultrafine endoscope with a 0.7 mm diameter for fine vessel imaging, the *ex vivo* IVPA/US imaging of a thoracic aorta (with an inner diameter of 1.15 mm) from an ApoE-mouse (35 weeks old) was carried out. After sacrificed by euthanasia, the mouse thoracic artery was excised and preserved in formaldehyde before IVPA/US imaging experiments [26]. The harvested artery was fixed in an agar phantom, and the experiments were conducted without the outer sheath. Then, a spiral scan from the proximal end to the distal end was conducted. After the IVPA imaging, the mouse thoracic artery was sectioned into slices and stained with Oil Red O for histological analysis. The stained tissue slices were captured using a color camera (AxioCam MRc 5, Carl Zeiss, Germany) mounted on a stereoscope (SteREO Lumar. V12, Carl Zeiss, Germany).

Two obtained cross-sectional IVPA images and US images of the thoracic aorta are shown in Fig. 4. Figure 4(a) showed the IVPA images of lipid distribution of the thoracic aorta, two white arrows showed the lipid imaged by the ultrafine IVPA endoscope (corresponding to the black arrows showed in histological result), and the US image of the aorta section is shown in Fig. 4(b) and the merged IVPA/US image is shown in Fig. 4(c). Compared with the corresponding histological stain result, the merged IVPA/US image indicated that the lipid reconstructed by the ultrafine IVPA endoscope was from the peri-adventital adipose of the aorta. The same result was observed earlier in this Letter.

The US images revealed the morphology of the thoracic aorta, which also has good consistency with the histological stain results. Since the aorta has been preserved in formalin, which may cause the deformation of the samples, several layer structures of the sample can be seen in histological images, which were also observed in the US images. In addition, the operating procedure of the frozen slice may change the

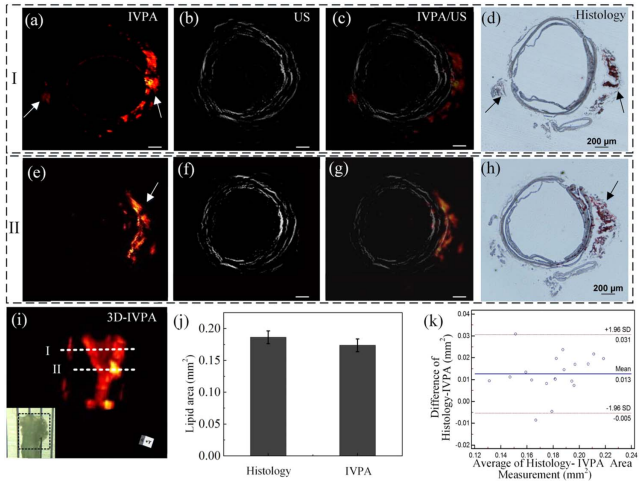

Fig. 4. PA and US images of the mouse thoracic aorta. (a), (e) Corresponding IVPA images of lipids at different cross sections (marked as I, II) in (i). (b), (f) Corresponding IVUS images of the cross sections I and II. (c), (g) Merged IVPA and IVUS images. (d), (h) Corresponding Oil Red O stain results. (i) Reconstructed 3D IVPA image of lipids. (j) Mean and mean square deviation error of the lipid area counted in IVPA imaging and histological staining. (k) Bland–Altman tests of IVPA and histology ($n = 20$). The scale bar is the same as the scale in Figs. 4(d) and 4(h).

morphology of the adipose tissue from the vascular wall, and this may lead to the difference between the IVPA/US images [Figs. 4(c) and 4(e)] and the histology stained slice results [Figs. 4(d) and 4(h)]. The 3D IVPA image of the lipid distribution in the mouse thoracic artery is shown in Figs. 4(i), and the lower left corner was the photograph of the mouse thoracic aorta (black dotted box was the imaging region).

The lipid area from the histological staining photograph and the PA images were measured by Image-Pro Plus (IPP) software (Media Cybernetics, USA). The mean and the mean square deviation error of the lipid area in the PA imaging and histological staining results are shown in Fig. 4(j). The average lipid areas were 0.1863 ± 0.04 mm^2 and 0.1737 ± 0.06 mm^2 for histological staining and IVPA imaging, respectively. Bland–Altman tests ($n = 20$) were performed to determine the agreement between them with Medcalc (Medcalc software, USA) in Fig. 4(k). The results also demonstrated a high degree of coherency between IVPA and histology staining results. These results indicated that the IVPA imaging was in good consistency with the histological staining in narrow artery lipid detection.

The diameter of the endoscope was critical to access the side branch to fulfill interventional strategy of bifurcation lesions or to evaluate the outcomes of bifurcation stenting. The total diameter of the ultrafine IVPA endoscope does not exceed 0.9 mm, even if the outer sheath is included, which is close to the diameters of the clinically used IVUS catheter with a diameter of 2.9 Fr (about 0.96 mm, Boston Scientific, USA) and the IVOCT catheter with a diameter of 2.7 Fr (about 0.89 mm, Dragonfly, C7, USA) (the outer sheath was counted in the diameter). Though there are some noises, which may cause the little artifacts in IVPA images, the ultrafine IVPA endoscope can still reconstruct most lipids in very fine vessel. In general, the ultrafine IVPA/US endoscope not only has the ability of lipid detection but can also locate the lipid position by comparing with US imaging.

In summary, we have designed and developed an ultrafine intravascular photoacoustic endoscope with a diameter of 0.7 mm, and the IVPA imaging of the stent and the mouse thoracic artery exhibited good reliability and consistency with histological staining results. The performance of the ultrafine endoscope illustrated its capability of fine coronary artery branches atherosclerotic detection. This ultrafine endoscope can also combine with other intravascular imaging methods such as IVOCT to provide more information about the coronary artery atherosclerotic. However, there is still more work to do to improve the performance of the ultrafine endoscope, such as improving the lateral resolution in this diameter by focusing the laser beam with fiber ball lens, and making the outer sheath suit with this endoscope for further *in vivo* experiments, which will promote the IVPA endoscope translation into clinical application.

Funding. National Natural Science Foundation of China (11774107, 61331001, 61627827, 61822505, 81571689, 81630046); Science and Technology Planning Project of Guangdong Province (2015B020233016); The Science and Technology Youth Talent for Special Program of Guangdong (2015TQ01X882).

Disclosures. The authors declare no conflicts of interest.

REFERENCES

1. D. S. Celermajer, C. K. Chow, E. Marijon, N. M. Anstey, and K. S. Woo, J. Am. Coll. Cardiol. **60**, 1207 (2012).
2. A. Taruttis and V. Ntziachristos, Nat. Photonics **9**, 219 (2015).
3. X. D. Leng, W. Chapman, B. Rao, S. Nandy, R. M. Chen, R. Rais, I. Gonzalez, Q. F. Zhou, D. Chatterjee, M. Mutch, and Q. Zhu, Biomed. Opt. Express **9**, 5159 (2018).
4. X. Li, J. C. Yin, C. H. Hu, Q. F. Zhou, K. K. Shung, and Z. P. Chen, Appl. Phys. Lett. **97**, 133702 (2010).
5. J. M. Yang, K. Maslov, H. C. Yang, Q. Zhou, K. K. Shung, and L. V. Wang, Opt. Lett. **34**, 1591 (2009).
6. A. Hussain, E. Hondebrink, J. Staley, and W. Steenbergen, Optica **5**, 1579 (2018).
7. J. Zhang, S. H. Yang, X. R. Ji, Q. Zhou, and D. Xing, J. Am. Coll. Cardiol. **64**, 385 (2014).
8. X. Huang, Y. Shi, Y. Liu, H. Xu, C. Xiao, J. Ren, and L. M. Nie, Opt. Lett. **42**, 2938 (2017).
9. B. Wang, J. L. Su, J. Amirian, S. H. Litovsky, R. Smalling, and S. Emelianov, Opt. Express **18**, 4889 (2010).
10. S. Chen, Z. Xie, T. Ling, L. Guo, X. Wei, and X. Wang, Opt. Lett. **37**, 4263 (2012).
11. D. Cai, G. Li, D. Xia, Z. Li, Z. Guo, and S. L. Chen, Opt. Express **25**, 20162 (2017).
12. P. Wang, T. Ma, M. N. Slipchenko, S. S. Liang, J. Hui, K. K. Shung, S. Roy, M. Sturek, Q. F. Zhou, Z. P. Chen, and J. X. Cheng, Sci. Rep. **4**, 6889 (2014).
13. X. Bai, X. Gong, W. Hau, R. Lin, J. Zheng, C. Liu, C. Zeng, X. Zou, H. Zheng, and L. Song, PLoS One **9**, e92463 (2014).
14. N. Wu, S. Q. Ye, Q. S. Ren, and C. H. Li, Opt. Lett. **39**, 2451 (2014).
15. X. R. Ji, K. D. Xiong, S. H. Yang, and D. Xing, Opt. Express **23**, 9130 (2015).
16. G. van Soest, E. Regar, and A. F. W. Vander Steen, Nat. Photonics **9**, 626 (2015).
17. B. Dong, S. Chen, Z. Zhang, C. Sun, and H. F. Zhang, Opt. Lett. **39**, 4372 (2014).
18. Y. Li, X. J. Gong, C. B. Liu, R. Q. Lin, W. Hau, X. S. Bai, and L. Song, J. Biomed. Opt. **20**, 065006 (2015).
19. J. Hui, Y. C. Cao, Y. Zhang, A. Kole, P. Wang, G. L. Yu, G. Eakins, M. Sturek, W. B. Chen, and J. X. Cheng, Sci. Rep. **7**, 1417 (2017).
20. M. Wu, G. Springeling, M. Lovrak, F. Mastik, S. iskander-rizk, T. Wang, H. M. M. Vanbeusekom, A. F. W. Vander Steen, and G. Van Soest, Biomed. Opt. Express **8**, 2 (2017).
21. Y. C. Cao, A. Kole, J. Hui, Y. Zhang, J. Y. Mai, M. Alloosh, M. Sturek, and J. X. Cheng, Sci. Rep. **8**, 2400 (2018).
22. Z. L. Piao, T. Ma, J. W. Li, M. T. Wiedmann, S. H. Huang, M. Y. Yu, K. K. Shung, Q. F. Zhou, C. S. Kim, and Z. P. Chen, Appl. Phys. Lett. **107**, 083701 (2015).
23. J. M. Yang, C. Li, R. Chen, Q. Zhou, K. K. Shung, and L. V. Wang, J Biomed. Opt. **19**, 066001 (2014).
24. K. Jansen, A. F. van der Steen, M. Wu, H. M. van Beusekom, G. Springeling, X. Li, Q. Zhou, K. K. Shung, D. P. de Kleijn, and G. van Soest, J. Biomed. Opt. **19**, 026006 (2014).
25. L. Wang, P. Lei, X. Wen, P. F. Zhang, and S. H. Yang, Opt. Express **27**, 12832 (2019).
26. M. J. Xu, P. Lei, J. Q. Feng, F. F. Liu, S. H. Yang, and P. F. Zhang, Chin. Opt. Lett. **16**, 031702 (2018).